Magnetic Resonance in Medicine

32-Channel self-grounded bow-tie transceiver array for cardiac MR at 7.0T

Thomas Wilhelm Eigentler[1,2] 🆔 | **Andre Kuehne**[3] 🆔 | **Laura Boehmert**[1] 🆔 |
Sebastian Dietrich[4] 🆔 | **Antje Els**[1] | **Helmar Waiczies**[3] 🆔 | **Thoralf Niendorf**[1,3,5] 🆔

[1]Berlin Ultrahigh Field Facility (B.U.F.F.), Max Delbrück Center for Molecular Medicine in the Helmholtz Association, Berlin, Germany

[2]Chair of Medical Engineering, Technische Universität Berlin, Berlin, Germany

[3]MRI.TOOLS GmbH, Berlin, Germany

[4]Physikalisch-Technische Bundesanstalt (PTB), Braunschweig and Berlin, Germany

[5]Experimental and Clinical Research Center (ECRC), a joint cooperation between the Charité Medical Faculty and the Max Delbrück Center for Molecular Medicine in the Helmholtz Association, Berlin, Germany

Correspondence

Thoralf Niendorf, Berlin Ultrahigh Field Facility (B.U.F.F.), Max Delbrück Center for Molecular Medicine in the Helmholtz Association, Robert-Roessle-Strasse 10, 13125 Berlin, Germany.
Email: thoralf.niendorf@mdc-berlin.de

Purpose: Design, implementation, evaluation, and application of a 32-channel Self-Grounded Bow-Tie (SGBT) transceiver array for cardiac MR (CMR) at 7.0T.

Methods: The array consists of 32 compact SGBT building blocks. Transmission field (B_1^+) shimming and radiofrequency safety assessment were performed with numerical simulations and benchmarked against phantom experiments. In vivo B_1^+ efficiency mapping was conducted with actual flip angle imaging. The array's applicability for accelerated high spatial resolution 2D FLASH CINE imaging of the heart was examined in a volunteer study (n = 7).

Results: B_1^+ shimming provided a uniform field distribution suitable for female and male subjects. Phantom studies demonstrated an excellent agreement between simulated and measured B_1^+ efficiency maps (7% mean difference). The SGBT array afforded a spatial resolution of $(0.8 \times 0.8 \times 2.5)$ mm^3 for 2D CINE FLASH which is by a factor of 12 superior to standardized cardiovascular MR (CMR) protocols. The density of the SGBT array supports 1D acceleration of up to R = 4 (mean signal-to-noise ratio (whole heart) ≥ 16.7, mean contrast-to-noise ratio ≥ 13.5) without impairing image quality significantly.

Conclusion: The compact SGBT building block facilitates a modular high-density array that supports accelerated and high spatial resolution CMR at 7.0T. The array provides a technological basis for future clinical assessment of parallel transmission techniques.

KEYWORDS

cardiovascular MRI, electrical dipole, parallel imaging, RF coil, transceiver array, ultrahigh field MRI

---

1 | INTRODUCTION

Advances in cardiovascular MR (CMR) at ultrahigh magnetic field strengths (UHF, $B_0 \geq 7.0$T) foreshadow some of the potential benefits to be expected as this technology moves to translational research and clinical science.[1,2] Transferring UHF-CMR into the clinic remains a major challenge since the advantages are sometimes hampered by concomitant physics-related phenomena. UHF-CMR is particularly susceptible to non-uniformities in the radiofrequency (RF) transmission field (B_1^+). To address this obstruction several reports refer to the development of enabling technology tailored for UHF-CMR.[3] Research directions for B_1^+ inhomogeneity compensation include RF pulse design and enabling multi-channel RF coil technology. Pioneering RF array developments for CMR at 7.0T include stripline-elements,[4] stripline waveguide like elements,[5] loop elements,[6-10] dipoles,[11,12] slot-antennas,[13] loop-dipoles,[14,15] and dipole building block elements.[16,17]

Dipole antenna configurations have gained increased attention for UHF-CMR. Electric dipoles run the trait of a linearly polarized current pattern, where RF energy is directed perpendicular to the dipole along the Poynting vector to the object under investigation resulting in a symmetrical, rather uniform excitation field with increased penetration depth.[14,16-18] At UHF-MRI linear (curl-free) current patterns provided by electric dipoles help to approach ultimate intrinsic signal-to-noise ratio (SNR).[19] Current dipole and loop-dipole RF arrays rely on geometrical decoupling limiting the number of transmitting (TX) elements that can be placed per unit area.[11,14,15] Yet, a high number of elements is favorable to increase the degrees of freedom and improve B_1^+ at a deep-seated cardiac region of interest (ROI).[20] For reception (RX) a high number of RF array elements afford parallel imaging with increased acceleration.[21] High-permittivity and low-loss dielectric materials facilitate dipole antenna shortening and are promising to provide sufficient decoupling allowing high channel count RF arrays.[16,22,23]

To summarize, RF arrays tailored for UHF-CMR should meet the requirements of patient safety, patient comfort, and ease of clinical use to harmonize the technical specifications with the clinical needs. This includes lightweight, flexibility, the capability to accommodate multiple body habitus and anatomical variants, a modular and multi-dimensional arrangement of RF building blocks together with a sensitive region large enough to cover the human heart.[24] Recent investigations demonstrated the feasibility of a Self-Grounded Bow-Tie (SGBT) building block at 7.0 T MRI.[23,25] The hallmark of this antenna type is its strong main lobe directivity and small size, based on a dielectrically filled housing for effective wavelength shortening and antenna size reduction.[23,26,27] Recognizing these opportunities it is conceptually appealing to pursue the development of an SGBT-based high-density TX/RX RF array tailored for UHF-CMR. To meet this goal this work reports on the design, implementation, evaluation, and application of a modular, lightweight 32-channel SGBT TX/RX array for CMR at 7.0 T. For this purpose, the proposed RF array is examined in electromagnetic field (EMF) simulations and benchmarked against phantom experiments. The feasibility of the RF array is demonstrated for high spatial resolution 2D CINE imaging of the heart in healthy subjects as a mandatory precursor to broader patient studies.

2 | METHODS

2.1 | Ethics statement

For the in vivo feasibility study, subjects without any known history of cardiac disease were included after approval by the local ethical committee (registration number EA1/256/19, Ethikausschuss am Campus Charité – Mitte, Berlin, Germany). Informed written consent was obtained from each volunteer prior to the study.

2.2 | RF antenna building block design

The RF antenna building block consists of an SGBT antenna with a dielectric-filled housing (Figure 1).[23,27] The SGBT dipole antenna has a strong main lobe directivity and limited back radiation due to the self-grounded backplane.[26] The antenna was manufactured with a 0.3 mm copper sheet, to ensure a mechanically robust setup. The additive manufactured housing is based on lithography (Form2, Formlabs, Somerville, MA, United States of America) and filled with deuterium oxide (D2O, 99.9%, $\varepsilon_r \approx 81$ at 297.2 MHz, Sigma Aldrich GmbH, Munich, Germany) as dielectric to shorten the effective RF wavelength and to reduce the overall antenna size. The building block surface facing the object under investigation consists of a 0.5 mm FR-4 sheet (Figure 1C). From the SGBT antenna tip, a parallel transmission line was connected to the tuning and matching network at the backside of the building block containing, a variable nonmagnetic ceramic capacitor (~1-23 pF, Voltronics Inc., Denville, NJ, United States of America) and a nonmagnetic air-core inductor (12.2 nH, Coilcaft Inc., Cary, IL, United States of America). The circuit network was covered with lithography-based manufactured housing for the individual element (Figure 1C,D).

2.3 | Cardiac array assembly

To constitute the high-density TX/RX cardiac array sixteen SGBT building blocks were combined to form the anterior section. Sixteen SGBT building blocks were integrated into the posterior section (Figure 2). For this purpose, the SGBT building blocks were placed next to each other as close as
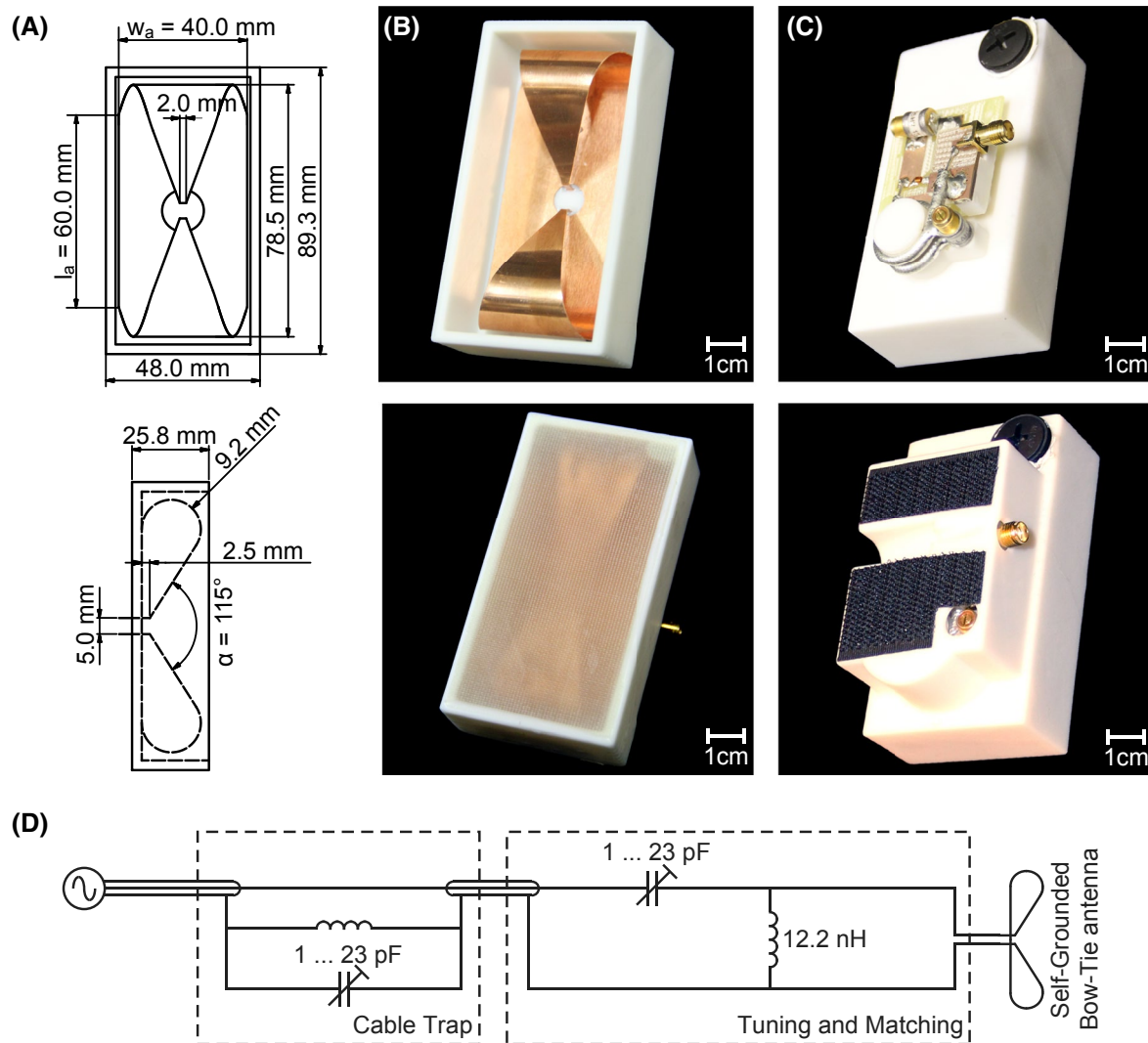
FIGURE 1 A, Schematic bottom view (top) and side view (bottom) of the SGBT antenna building block including the dimensions. B, Manufactured SGBT antenna inside the open (top) and closed (bottom, 0.5 mm FR-4), additive manufactured housing. C, Backside of the building block showing the electrical circuit and the cover including the hook-and-loop fastener used to connect building blocks for the assembly of the 32 channel TX/RX array (bottom). D, Schematic visualization of the circuit including the tuning and matching and the solenoid cable trap with 1.5 windings.

possible with three rows of building blocks along the head-feet direction. A shift of the array to the left side of the subject was introduced to place the center of the antenna array above the heart (Figure 2A). The anterior RF building blocks were fixed by hook-and-loop fasteners allowing a flexible connection between the building blocks and a close-fitting to the upper torso, regardless of sex or body mass index (BMI). For the posterior section, a holder system was made from acrylonitrile butadiene styrene (ABS) material using a rapid prototyping system (BST 1200es, Dimension Inc., Eden Prairie, MN, USA). The holder system accommodated the SGBT building blocks and was integrated into the patient table cushions, hence no extra free magnet bore space is consumed. To reduce EMF reflections, a hydrogel pad was placed between the anterior and posterior sections of the RF array and the object under investigation (Figure 2C). The hydrogel ($\varepsilon_r \approx 82$,

$\sigma \approx 0.17$ S/m) consists of xanthan (0.4% mass fraction, Roth AG, Arlesheim, Switzerland), locust bean gum (0.4% mass fraction, Merck KGaA, Darmstadt, Germany), and agarose (0.2% mass fraction, Roth AG, Arlesheim, Switzerland) filled in a vacuum-sealed bag.[28] For RF safety and to avoid excessive local specific absorption rate (SAR) in the vicinity of the conductors, the thickness (≥ 5 mm) of the hydrogel pad and the design of the building block casing assures a minimum distance between the RF array and the object.

2.4 | Hardware

MR experiments were conducted on a 7.0T whole-body MR scanner (MAGNETOM, Siemens Healthineers, Erlangen, Germany) equipped with an 8 kW RF power amplifier (RFPA,
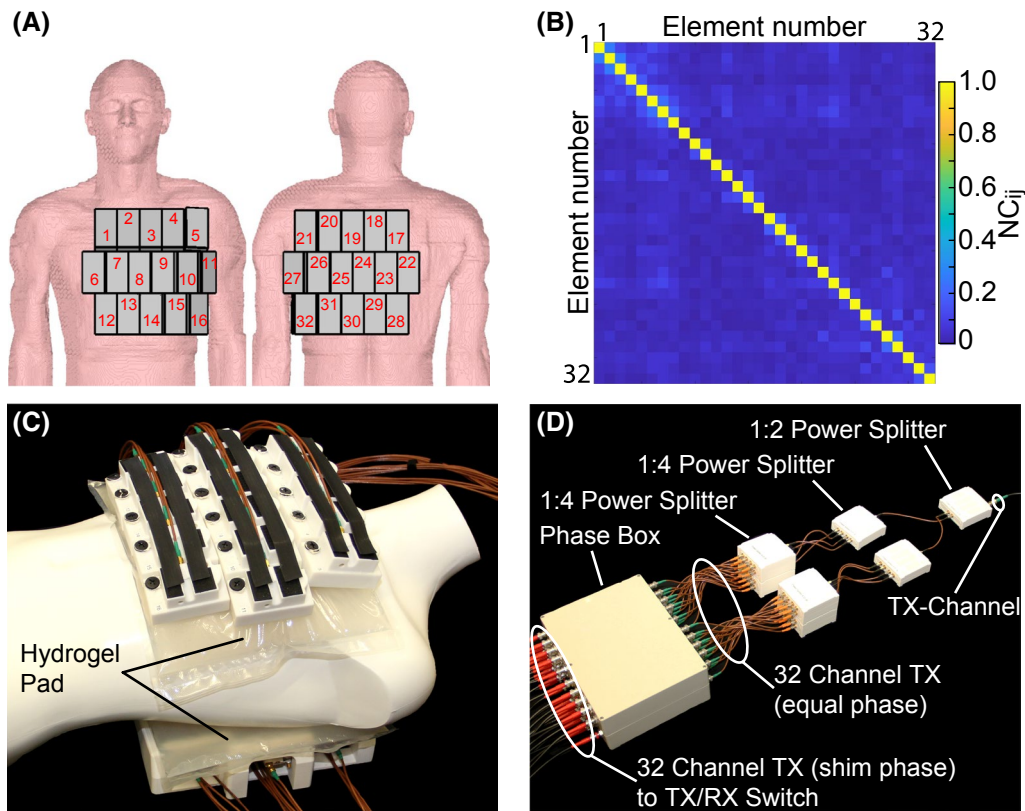
FIGURE 2 A, Schematic view of the antenna arrangement for the 32-channel cardiac array on the human voxel model Duke together with the channel nomenclature. B, Averaged, measured noise correlation (NC) matrix of the 32-channel SGBT building block array of all subjects involved in the CMR study. C, Implementation used in the feasibility study with the anterior section fixed by hook-and-loop fasteners. The posterior section was placed in an additive manufactured holder system and was integrated into the patient table's cushions. Hydrogel pads were used to improve an electromagnetic impedance match to reduce electromagnetic reflections between the building blocks and the object under investigation. D, Cascade of one 1:2, two 1:4, and eight 1:4 power splitters (Power Splitter 297.2 MHz, MRI.TOOLS GmbH, Berlin, Germany) resulting in a 32-channel equal phase transmit (TX) signal feeding the phase box, containing single-channel phase adjustments (α_{exc}) by using phase-shifting coaxial cables. The phase-shifted TX signal is connected to four multi-purpose interface boxes equipped with TX/RX switches and integrated low-noise preamplifiers (Stark Contrast, Erlangen, Germany)

Stolberg HF-Technik AG, Stolberg-Vicht, Germany) and a gradient system with a maximum slew rate of 170 mT/m/ms and gradient strength of 38 mT/m. To drive the RF array, the transmit signal was divided into 32 equal amplitude signals using a cascade of one 1:2, two 1:4, and eight 1:4 Wilkinson power splitters with lumped elements (Power Splitter 297.2 MHz, MRI.TOOLS GmbH, Berlin, Germany). The phase adjustments (α_{exc}) of the individual channels were incorporated by using phase-shifting coaxial cables (Figure 2D). The 32-channels of the proposed cardiac array were connected to the MR signal chain using four eight-channel multi-purpose interface boxes with transmit/receive switches and integrated low-noise preamplifiers (Stark Contrast, Erlangen, Germany).

2.5 | EMF simulations

EMF simulations were performed using the finite integration technique (FIT) solver of CST Microwave Studio (CST Studio Suite 2020, Dassault Systèmes, Vélizy-Villacoublay Cedex,

France) with a broadband excitation at 297.2 ± 50.0 MHz. The simulations were performed for a rectangular phantom setup ($156 \times 374 \times 318$ mm^3, $\varepsilon_r = 48$, $\sigma = 0.47$) and for the human voxel models Ella and Duke from the virtual population.[29] The voxel models were used from the upper neck to the navel at a resolution of $1.0 \times 1.0 \times 1.0$ mm^3. The dielectric material specification of the phantom was measured with an open-end coaxial probe.[30] Tissue properties were defined at 297.2 MHz according to the tissue database of the IT'IS Foundation.[31] All simulations were performed within a model of the MRI bores' RF shield. The simulation resolution was kept below $4.0 \times 4.0 \times 4.0$ mm^3 for all configurations. B_1^+ efficiency was calculated by dividing the magnetic transmit RF field by the root mean square of the input power in kW.

2.6 | Evaluation and optimization of SGBT

The antenna dimensions width (w_a), length (l_a), and dihedral angle (α) were investigated using CST Microwave Studio

to achieve the highest possible B_1^+ efficiency divided by the building blocks' footprint (B_1^+ efficiency to footprint ratio). For this purpose, the SGBT building block and the hydrogel pad were placed centrally above the heart of the human voxel models (Ella and Duke) and the lateral wall of the heart was used as ROI as indicated in Figure 3A.

2.7 | Co-simulation, transmission field shaping, and SAR calculation

A co-simulation was performed in MATLAB 2019b (MathWorks, Natick, MA) for channel-wise tuning and matching (f = 297.2 MHz) with a lossy capacitance (equivalent series resistance = 0.2 Ω, equivalent series inductance = 1 nH) and a lossy inductance (Q = 45).[32] EMF simulation results were scaled accordingly and together with the material matrices used to calculate B_1^+ fields and SAR distributions averaged over 10g tissue or material (SAR_{10g}). To reduce the computational effort for the B_1^+ shimming approach the channel-wise transmission field was regridded to an isotropic resolution of $4.0 \times 4.0 \times 4.0$ mm[3] and SAR_{10g} was compressed using virtual observation points (VOPs) at an overestimation factor of 0.01.[33,34] RF power loss calculation was performed using a quadratic-form-based framework for loss analysis in multichannel arrays.[35] All results referring to the power absorption were calculated without losses in the signal chain, ie, the reference plane was at the input of the balun on the SGBT antenna. The intrinsic transmit efficiency and the intrinsic SNR distributions were calculated as an optimum superposition of B_1^+ and B_1^- with respect to the power absorbed by the voxel model. Assuming complete dominance of sample noise, this yields a theoretical upper bound for the B_1^+ shimming performance and is proportional to image SNR.[32] The intrinsic measures were contrasted with the realistic transmit efficiency and the realistic SNR with considering all coil losses. The performance ratio (%) of the RF array reveals the ratio of the intrinsic and the realistic B_1^+ and B_1^- superpositions. The values derived in this way can be used to quantitatively compare expected SNR and transmit efficiency of different arrays and to assess theoretical electromagnetic upper bounds.[36,37]

EMF shaping was performed using a combined approach for Ella and Duke, where the minimum B_1^+ in the ROI is maximized by using the target function

$$f\left(exc\right) = min\left(B_{1Ella}^+\left(exc\right)\right) + \delta \cdot min\left(B_{1Duke}^+\left(exc\right)\right) - \lambda \cdot max\left(VOP_{Ella}\left(exc\right) + VOP_{Duke}\left(exc\right)\right)$$

with the B_1^+ scaling factor ($\delta = 1\ldots4$) and VOPs scaling factor ($\lambda = 0.001\ldots5$). The phase optimization was performed with a generic algorithm implemented in the global optimization toolbox of MATLAB 2019b.

2.8 | Phantom experiments for EMF simulations validation

To examine the RF characteristics of the cardiac array and of the signal chain, bench measurements were performed using a four-channel vector network analyzer (ZNB 4, Rohde & Schwarz, Memmingen, Germany) in conjunction with a switching matrix (ZN-Z84, Rohde & Schwarz, Memmingen, Germany).

A custom-made rectangular phantom ($156 \times 374 \times 318$ mm[3]) consisting of deionized water, sucrose (1425.7 g/L), NaCl (58.7 g/L), agarose (25 g/L, and CuSO4 (0.75 g/L) was used to validate the EMF simulations obtained for the 32-channel SGBT antenna building block array. Simulated B_1^+ efficiency distributions were benchmarked against measured B_1^+ efficiency maps for transversal slices through each of the three SGBT antenna building block rows. For this evaluation, two-phase setting modes were used: (1) the equal phase excitation ($\alpha_1 \ldots \alpha_{32} = 0°$) and (2) the phase shim excitation (α_{exc}) obtained with the proposed optimization algorithm.

B_1^+ efficiency field measurements were conducted with a non-slice-selective actual flip angle imaging (AFI) method (spatial resolution = $1.0 \times 1.0 \times 2.5$ mm[3], rectangular pulse PD = 1 ms TE = 2.19 ms, TR_1 = 42 ms, TR_2 = 122 ms, BW = 500 Hz/Px, nominal FA = 50°, V_{ref} = 520 V, 64 slices) and calculated offline in MATLAB 2019b.[38] Measured losses in the signal chain of the MRI system were considered in the simulation results. Pixel-by-pixel difference maps were calculated using a in plane resolution of 1.0×1.0 mm[2] where the B_1^+ mask ($B_1^+ \geq 4$ µT/$\sqrt{kW}$ in simulation without losses) was used for cropping low signal areas. An ROI was defined in the phantom to evaluate the simulation and measurement results.

2.9 | Volunteer studies

The in vivo study was performed in seven healthy subjects (three females, four males; age = 29-59; average BMI = 23,8 ± 2,1 kg/m²; minimum BMI = 20,2 kg/m²; maximum BMI = 27.2 kg/m²). The study design contained B_1^+ efficiency mapping (two subjects), 2D CINE FLASH imaging (seven subjects), assessment of spatial resolution enhancement (four subjects), and parallel imaging (four subjects). For retrospective cardiac gating and prospective cardiac triggering electrocardiogram (ECG) electrodes and an MR stethoscope (EasyACT, MRI.TOOLS GmbH, Berlin, Germany) were placed between the hydrogel pad and the anterior chest wall.

To facilitate 3D flip angle measurement, a radial phase encoding (RPE) gradient-echo acquisition scheme was modified to acquire two interleaved TRs, which enables the computation of absolute B_1^+ efficiency maps according to the AFI approach (RPE-AFI).[38] RPE-AFI was obtained with: spatial resolution = $5.0 \times 5.0 \times 5.0$ mm[3], rectangular pulse PD = 0.5 ms, TE = 2.04 ms, TR_1 = 10 ms, TR_2 = 50 ms, nominal
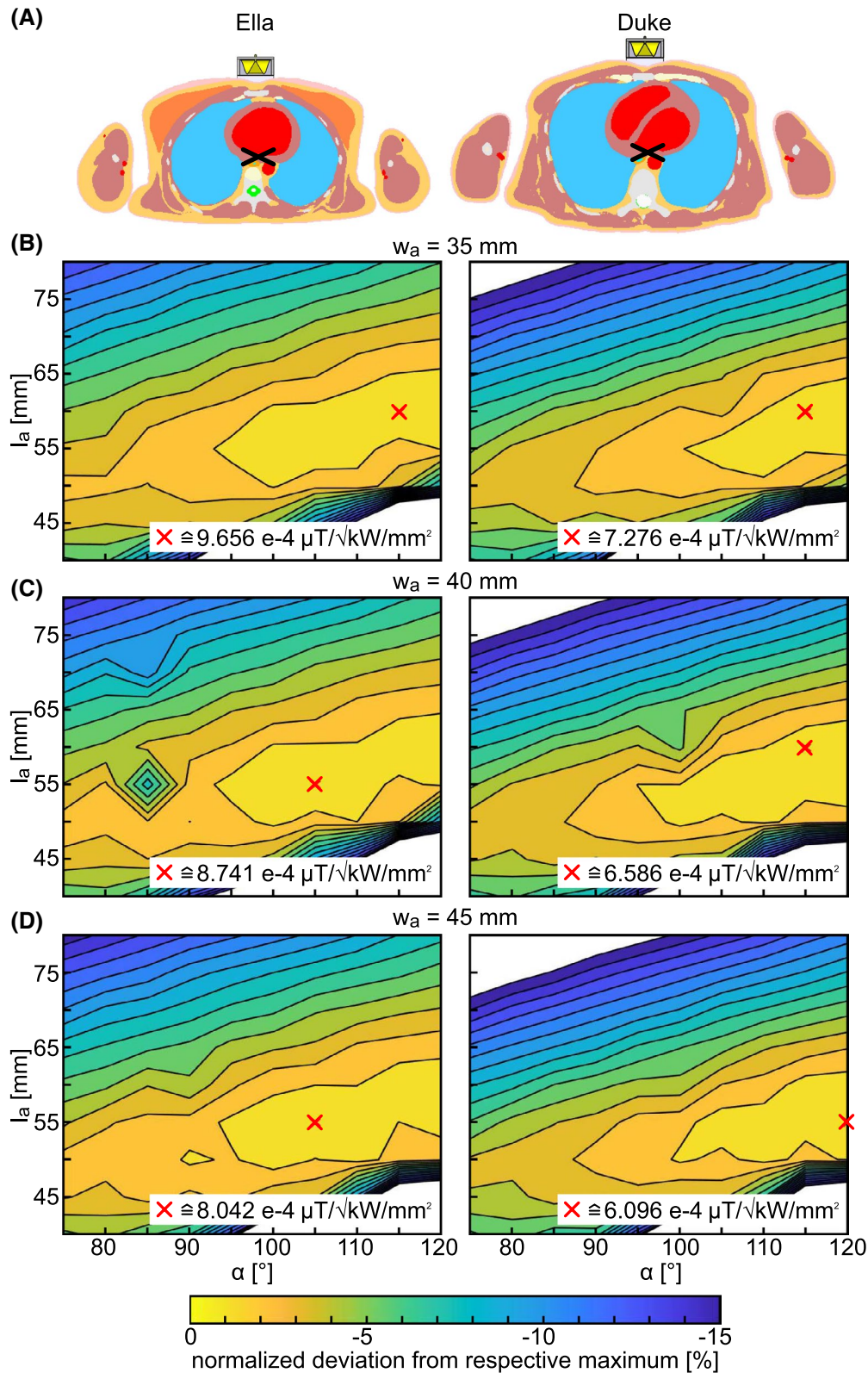
FIGURE 3 Summary of the results obtained for the optimization of the SGBT antenna geometry using the human voxel model Ella and Duke. A, The ROI used for the B_1^+ efficiency calculation within the optimization is marked by the black cross. The normalized deviation [%] from the respective maximum of the ratio between the B_1^+ efficiency and the footprint of the building block is shown for a parametric sweep ($\alpha = 75°\ ...\ 120°$ and $l_a = 40$ mm ... 80 mm) and an antenna width of $w_a = 35$ mm (B), $w_a = 40$ mm (C), and $w_a = 45$ mm (D). The maximum B_1^+ efficiency to building block footprint ratio is highlighted by a red cross for each parameter sweep

FA = 66°, V_{ref} = 520 V, and 12 readouts per radial line following Dietrich S. et al.[39]

2D CINE FLASH imaging of the heart was performed to obtain short axis (SAX), two-chamber (2CV), three-chamber (3CV), and four chamber (4CV) views of the human heart (spatial resolution = $1.1 \times 1.1 \times 2.5$ mm^3, TE = 2.09 ms, TR = 4.55 ms, GRAPPA R = 2, views per segment = 10, cardiac phases = 30, BW = 446 Hz/Px, nominal FA = 22°, V_{ref} = 520 V). Imaging parameters were slightly adjusted for subject 1, subject 3, and subject 7 (TE = 2.14-2.17 ms, TR = 4.72-5.58 ms). The noise correlation matrix was derived from averaging noise pre-scans obtained for each subject without RF excitation.[40]

2D CINE FLASH imaging targeting the 4CV and the SAX were performed for spatial resolutions: (1) $1.8 \times 1.8 \times 6.0$ mm^3 according to standardized protocols used in CMR practice[41] (TE = 1.75 ms, TR = 3.96 ms, views per segment = 10, cardiac phases = 30), (2) $1.4 \times 1.4 \times 4.0$ mm^3 (TE = 1.84 ms, TR = 4.14 ms, views per segment = 10, cardiac phases = 30), (3) $1.1 \times 1.1 \times 2.5$ mm^3 (see above), and (4) $0.8 \times 0.8 \times 2.5$ mm^3 (TE = 2.11 ms, TR = 4.75 ms, GRAPPA R = 2, views per segment = 10, cardiac phases = 30). The normalized signal intensity profile along a circumferential trajectory inside the myocardium was plotted for a mid-ventricular SAX at end-diastole for four subjects. The results were labeled using the common segmentation of the myocardium.[42]

The antenna arrays' parallel imaging performance was evaluated using acceleration factors of up to R = 6 and GRAPPA reconstruction.[43] Prospective imaging of the 4CV and SAX was used at a resolution of $1.1 \times 1.1 \times 2.5$ mm^3 (TE = 2.5 ms, TR = 4.55 ms, views per segment = 10, BW = 446 Hz/Px, and a nominal FA = 22° at V_{ref} = 520 V). The phase encoding direction was kept the same for all reduction factors within a subject (4CV-AP: subject 2 and 5; 4CV-RL: subject 4 and 6; SAX-AP: subject 2 and 4; SAX-HF: subject 5 and 6). Offline image reconstruction was performed in MATLAB 2019b.[44] Pseudo replicas (500) were used to calculate the SNR scaled images and geometry factor (g-factor) maps. Contrast-to-noise ratio (CNR) was calculated by subtracting the SNR values of the myocardium from the SNR values of the ventricular blood pool in the 4CV and SAX.[45] The acquired data was assessed for each individual subject ($SNR_{whole-heart,mean}$, $SNR_{myocardium,mean}$, $g-factor_{whole-heart,mean}$, $g-factor_{whole-heart,max}$, and CNR) and statistically analyzed for all subjects enrolled in the parallel imaging study.

3 | RESULTS

3.1 | RF antenna building block design and characteristics

The results of the EMF simulations are summarized in Figure 3, suggesting a small antenna width for an enhanced B_1^+ efficiency to footprint ratio. Coupling between the elements, on the other hand, favors an increased antenna width, resulting in a lower coupling between SGBT building blocks in an RF array. The final antenna design (w_a = 40.0 mm, l_a = 69.0 mm, α = 115.0°) was defined as a trade-off between the B_1^+ efficiency to footprint ratio and the decoupling behavior. The result was deduced from the EMF simulations with the human voxel model Duke, because of the reduced B_1^+ efficiency compared to Ella (Figure 3). Following the implementation, the SGBT building block exhibits a weight of 156 g and a size of $89.3 \times 48.0 \times 25.8$ mm^3. This SGBT building block configuration allows a nearest-neighbor coupling of $S_{ij} \leq -11.2$ dB at 0° relative angle and 0 mm distance between the SGBT building blocks when placed on the thorax of the human voxel models Duke ($S_{ij} = -12.7$ dB) and Ella ($S_{ij} = -11.2$ dB). The decoupling performance relies on geometrical decoupling and allows the use in an RF array without additional decoupling measures (eg, impedance transformation network and preamplifier decoupling). In comparison, EMF simulations with w_a = 35 mm and w_a = 45 mm revealed a coupling of $S_{ij} \leq -10.6$ dB and $S_{ij} \leq -12.3$ dB. The power absorption analysis of a single channel revealed that on average 61% and 71% of the input is absorbed in the body of Ella and Duke for the 32-channel array. The other losses are comprised of a material including the hydrogel pad (20-26%), coupling (8-11%), and lumped element losses (~1%).

3.2 | Cardiac array assembly

The anterior and posterior sections consist of sixteen SGBT building blocks each, covering a surface area of about 686 cm², respectively (Figure 2A). The total weight of the anterior section is approximately 2.5 kg. In the experimental setup the reflection and the coupling coefficient were found to be $S_{ii} < -10.2$ dB and $S_{ij} < -14.1$ dB. Figure 2B shows the noise correlation matrix which revealed a value of −0.258 or below within the array for all subjects.

3.3 | Hardware

The power splitters introduced losses of −0.27 dB for the 1:2 and −0.49 dB for the 1:4 with a maximum phase error of 1° each. The phase cables were capsulated in a box and manufactured with less than 2.2° phase deviation. Including all other parts of the system (cables between the described elements, the antenna cables, the TX/RX switch boxes, and the phase cables) the losses were found to be −5.15 dB at a cumulative worst-case phase error of 9.9°.

3.4 | Co-simulation, transmission field shaping, and SAR calculation

Numerical simulations of the 32-channel RF array revealed a reflection of $S_{ii} < -27$ dB and coupling of $S_{ij} < -12$ dB. The factor δ of the proposed mixed B_1^+ shimming within the heart of Ella and Duke allowed a B_1^+ efficiency gain for Duke at the expense of Ella. Dependent on the B_1^+ scaling factor δ and the VOPs scaling factor λ an optimum phase set was calculated maximizing the minimum B_1^+ of both voxel models. The optimized phase set ($\alpha_{exc} = -[0; 275; 241; 191; 135; 48; 0; 241; 204; 164; 128; 310; 273; 239; 169; 108; 0;$
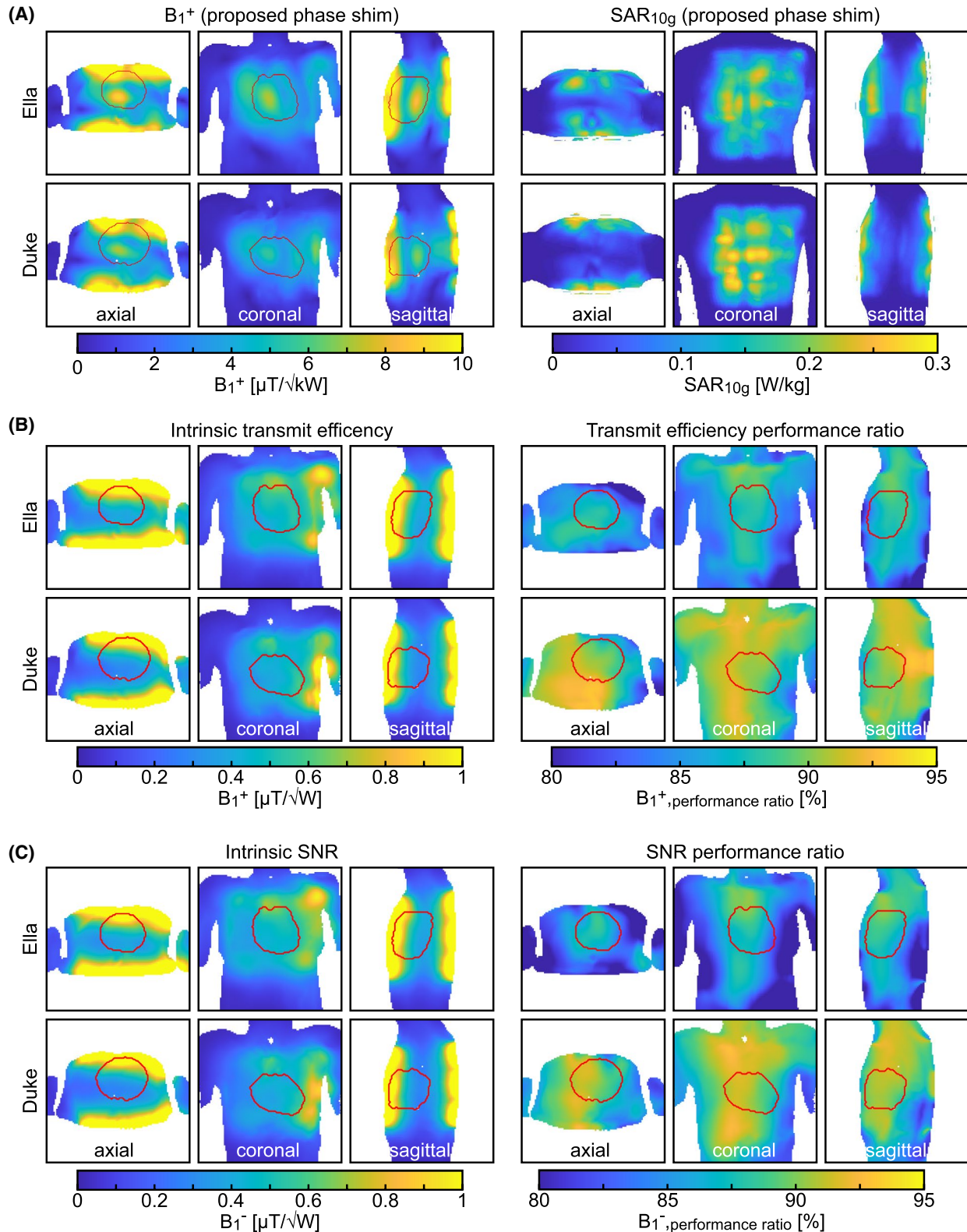
FIGURE 4 Summary of results obtained from the proposed optimized phase shim excitation (α_{exc} = -[0; 275; 241; 191; 135; 48; 0; 241; 204; 164; 128; 310; 273; 239; 169; 108; 0; 34; 33; 24; 9; 97; 126; 135; 115; 61; 38; 95; 82; 32; 311; 0]°) using the human voxel models Ella and Duke. A, B_1^+ efficiency is visualized for three orthogonal slices through the center of the cardiac ROI (highlighted in red). SAR_{10g} is visualized as a maximum projection for three orthogonal views. For Ella, the simulations revealed (mean ± SD [min]) B_1^+ = (6.2 ± 1.8 [3.4]) μT/$\sqrt{kW}$ and $SAR_{10g,max}$ = 0.25 W/kg. Duke showed B_1^+ = (5.6 ± 1.9 [2.8]) μT/$\sqrt{kW}$ and $SAR_{10g,max}$ = 0.30 W/kg. B, Intrinsic transmit efficiency and transmit efficiency performance ratio for the three orthogonal slices through the center of the cardiac ROI for Ella and Duke. For Ella, the intrinsic transmit efficiency revealed (mean ± SD [min]) B_1^+ = (0.68 ± 0.27 [0.36]) μT/$\sqrt{W}$ and $B_{1,performance\ ratio}^+$ = (87.4 ± 1.2 [82.7])%. For Duke, B_1^+ = (0.61 ± 0.31 [0.24]) μT/$\sqrt{W}$ and $B_{1,performance\ ratio}^+$ = (89.9 ± 1.4 [83.2])% was obtained. C, The intrinsic SNR and SNR performance ratio for three orthogonal slices through the cardiac ROI of Ella and Duke. For Ella, an intrinsic SNR (mean ± SD [min]) of B_1^- = (0.66 ± 0.25 [0.36]) μT/$\sqrt{W}$ and $B_{1,performance\ ratio}^-$ = (87.2 ± 1.5 [82.0])% was observed. For Duke, B_1^- = (0.60 ± 0.30 [0.26]) μT/$\sqrt{W}$ and $B_{1,performance\ ratio}^-$ = (90.1 ± 1.4 [85.3])% was estimated

34; 33; 24; 9; 97; 126; 135; 115; 61; 38; 95; 82; 32; 311; 0]°) corresponding to δ = 2.0 and λ = 0.025 showed both, a fair balance of the B_1^+ efficiency results of Ella and Duke with considerable low SAR_{10g}.

Figure 4A shows the B_1^+ efficiency distribution within the heart of the human voxel models for the proposed optimized phase shim excitation. A B_1^+ efficiency distribution of (mean ± SD [min]) (6.2 ± 1.8 [3.4]) μT/$\sqrt{kW}$ for Ella and (5.6 ± 1.9 [2.8]) μT/$\sqrt{kW}$ for Duke was obtained. The SAR_{10g} distributions (Figure 4A) were normalized to an average total power of 1.0 W and demonstrate a maximum of 0.30 W/kg for both voxel models (0.25 W/kg for Ella and 0.30 W/kg for Duke). Considering the described hardware losses in the RF chain and a maximum allowed SAR_{10g} of 20 W/kg in the first level controlled mode, the input power was limited to 8.1 W per channel including a safety factor of 1.7.[46] The intrinsic transmit efficiency revealed (mean) 0.68 μT/$\sqrt{W}$ for Ella and 0.61 μT/$\sqrt{W}$ for Duke, while the realistic transmit efficiency was 0.59 μT/$\sqrt{W}$ for Ella and 0.55 μT/$\sqrt{W}$ for Duke, corresponding to a transmit efficiency performance ratio of 87.4% for Ella and 89.9% for Duke. The intrinsic SNR revealed 0.66 μT/$\sqrt{W}$ for Ella and 0.60 μT/$\sqrt{W}$ for Duke, while the realistic SNR was 0.58 μT/$\sqrt{W}$ for Ella and 0.54 μT/$\sqrt{W}$ for Duke. The SNR performance ratio was found to be 87.2% for Ella and 90.1% for Duke. The power absorption analysis of α_{exc} demonstrated that 65% and 74% of the input power is absorbed in the body of Ella and Duke. The other losses are comprised of 13-16% material including the hydrogel pad, 10-16% coupling, and 1% lumped element losses.

3.5 | Phantom experiments for EMF simulations validation

The simulated and measured B_1^+ efficiency maps showed a good quantitative agreement with the signal chain losses and the patient table cable losses of −6.37 dB (an additional −1.22 dB on top of the −5.15 dB losses) being included. Figure 5 shows the data for three slices through the phantom. The absolute (simulation − measurement) voxel difference obtained for all three slices was found to be (mean ± SD)

(−0.26 ± 0.45) μT/$\sqrt{kW}$ for an equal phase excitation and (−0.01 ± 0.50) μT/$\sqrt{kW}$ for the proposed optimized phase excitation. The difference relative to the simulation results is (−6.1 ± 12.3)% and (−2.2 ± 14.5)% for the equal and the proposed phase excitation (α_{exc}). The B_1^+ efficiency distribution within the ROI in Figure 5C shows (mean ± SD [min]) (4.30 ± 0.34 [3.34]) μT/$\sqrt{kW}$ for the simulation and (3.90 ± 0.44 [2.43]) μT/$\sqrt{kW}$ for the measurement.

3.6 | Volunteer study

Figure 6 shows in vivo flip angle maps and the corresponding thresholded B_1^+ efficiency distributions (FA ≤ 15°) for sagittal, coronal, and transversal views through the heart. In vivo B_1^+ efficiency (mean ± SD) within the cardiac ROI was 2.8 ± 0.9 μT/$\sqrt{kW}$ for the female (subject 4) and 2.3 ± 0.7 μT/$\sqrt{kW}$ for the male (subject 5). For comparison with the simulation results (Ella: 6.2 ± 1.8 μT/$\sqrt{kW}$; Duke: 5.6 ± 1.9 μT/$\sqrt{kW}$), the in vivo data are scaled by the measured losses (−6.37 dB) and correspond to 5.8 μT/$\sqrt{kW}$ for the female subject and 4.8 μT/$\sqrt{kW}$ for the male subject as a mean value for the cardiac ROI.

Figure 7 shows the 4CV, 3CV, 2CV, and SAX views of the heart obtained from 2D CINE FLASH using the optimized phase setting (α_{exc}). For the acquisition, an in-plane spatial resolution of 1.1 × 1.1 mm² and a slice thickness of 2.5 mm were used. The image quality over all subjects included in our feasibility study was consistent without major signal voids due to destructive interferences.

4CV and SAX views of the heart at increasing spatial resolutions are shown in Figure 8. The overall image quality and enhancements in the spatial resolution enabled the visualization of fine subtle anatomic structures including the compact layer of the right ventricular free wall and the remaining trabecular layer. Pericardium, mitral, and tricuspid valves and their associated papillary muscles, and trabeculae are identifiable. The high spatial resolution protocol (0.8 × 0.8 × 2.5 mm³) presents a 12-fold improvement in the spatial resolution versus a standardized clinical CMR protocol.[41] A normalized signal intensity distribution obtained for the left ventricular myocardium
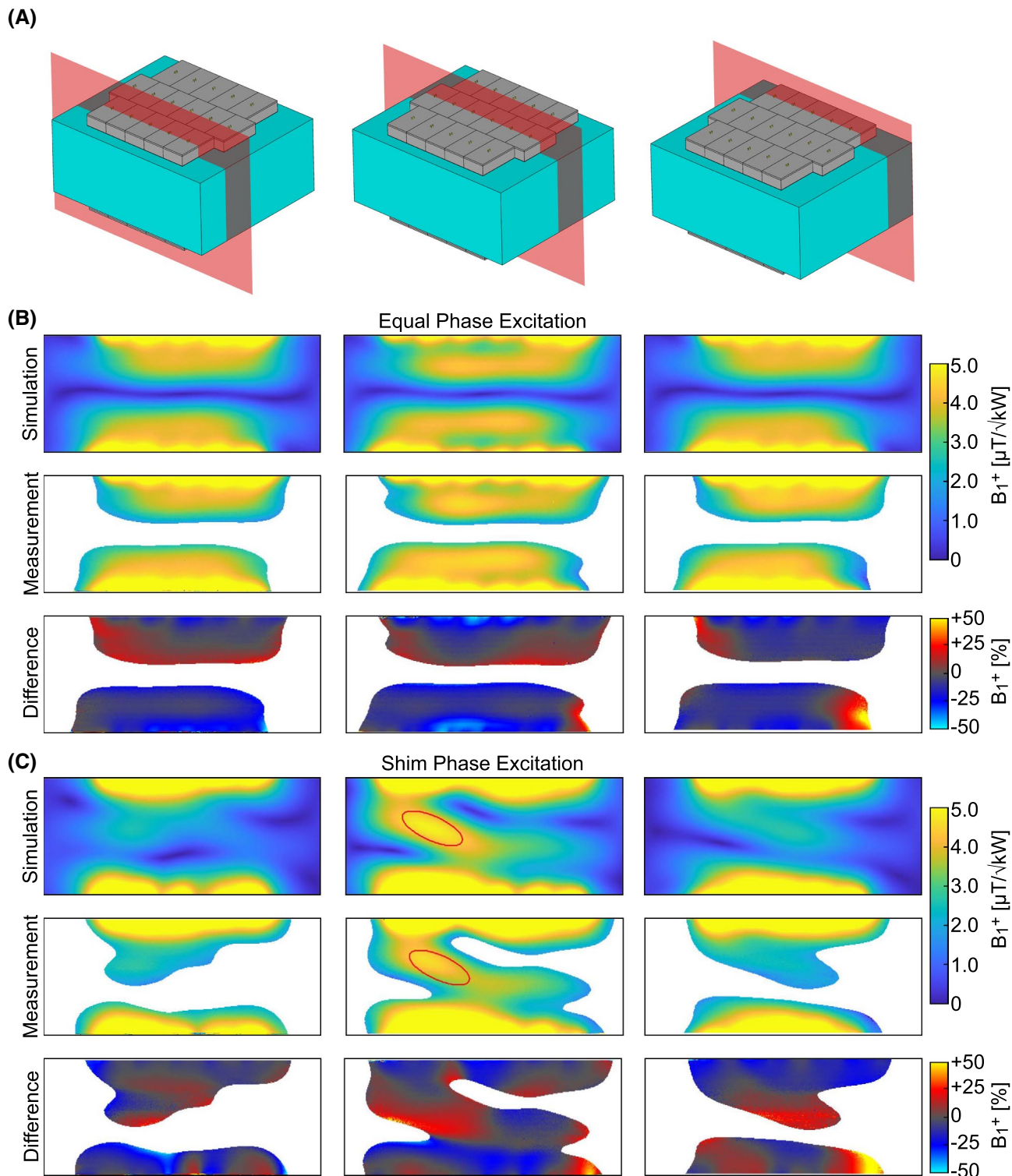
FIGURE 5 A) Illustration of the setup and slice positioning (slice 1-3) used for B_1^+ efficiency simulations and measurements. B_1^+ distribution obtained for equal phase excitation ($\alpha_1 \ldots \alpha_{32} = 0°$) (B) and proposed optimized phase shim excitation (α_{exc}) (C), including B_1^+ efficiency simulation results, B_1^+ efficiency mapping, and relative difference map in percent. For the measurement, a 3D AFI (spatial resolution = $1.0 \times 1.0 \times 5.0$ mm^3, TE = 1.94 ms, TR$_1$ = 29 ms, TR$_2$ = 109 ms, nominal FA = 50°, V$_{ref}$ = 520 V, 64 slices) was used. For the ROI marked in red, the optimized phase shim excitation (α_{exc}) shows (mean ± SD [min]) $B_1^+ = (4.30 \pm 0.34 \, [3.34])$ µT/$\sqrt{kW}$ for the simulation and $B_1^+ = (3.90 \pm 0.44 \, [2.43])$ µT/$\sqrt{kW}$ for the measurement

is shown in Figure 8C for each spatial resolution. The results show no major signal voids for the SAX and a signal intensity variation of approximately ± 50% with the lowest signal being found in the lateral wall of the left ventricle.

Figure 9 shows a dataset including SNR maps and g-factor maps for R = 2 to R = 6. The spatial resolution ($1.1 \times 1.1 \times 2.5$ mm^3) presents a 6-fold improvement in the spatial resolution versus a standardized clinical CMR protocol.[41] For
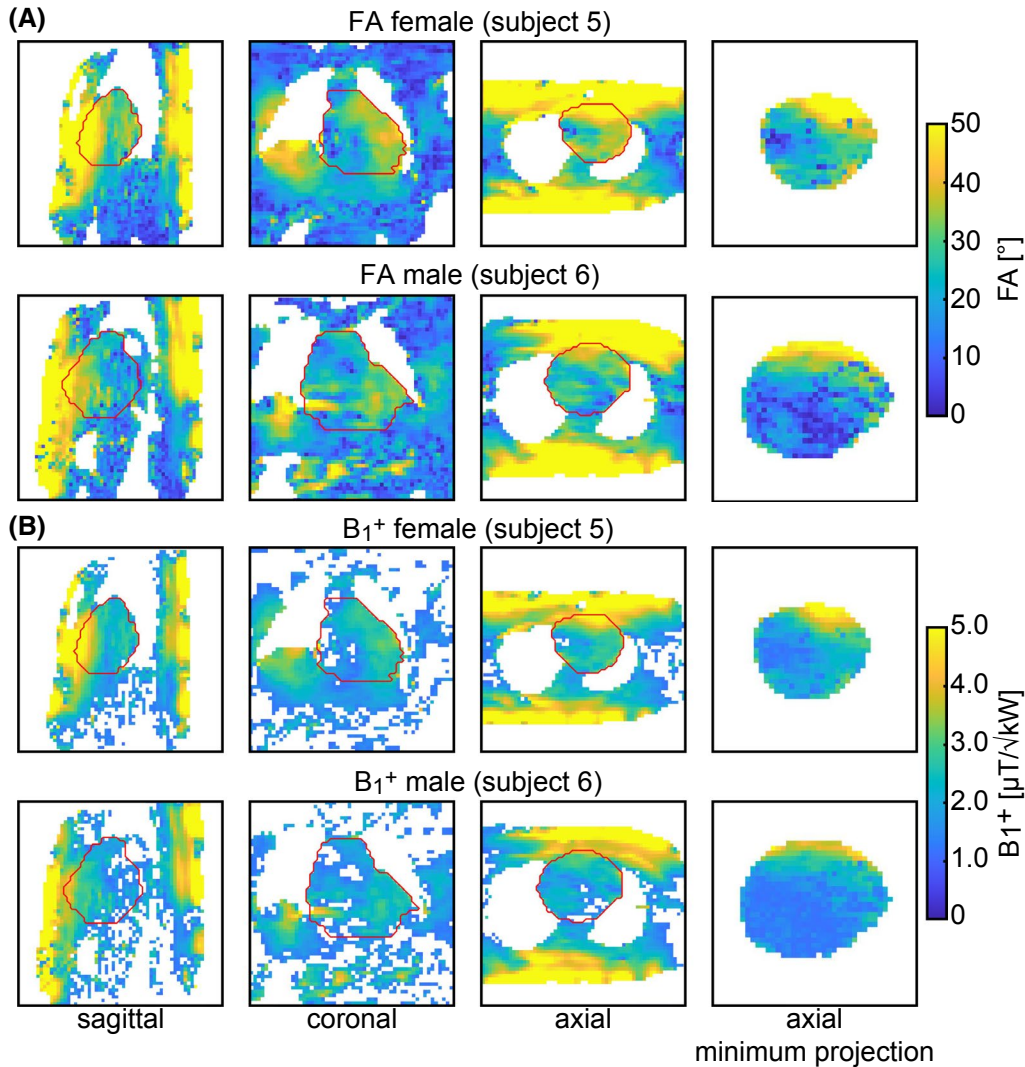
FIGURE 6 A, In vivo flip angle (FA) maps acquired with a 3D radial sampled free-breathing AFI (spatial resolution = $5.0 \times 5.0 \times 5.0$ mm^3, rectangular pulse PD = 0.5 ms TE = 2.04 ms, TR$_1$ = 10 ms, TR$_2$ = 50 ms, nominal FA = 66°, V$_{ref}$ = 520 V, and 12 readouts per radial line) in a female and male human subject. B, B_1^+ efficiency maps calculated based on FA results with FA $\leq$ 15° rejected. FA and B_1^+ are shown for a sagittal (first column), coronal (second column), and axial slice (third column) through the heart (cardiac ROI highlighted in red) as well as a minimum projection in the axial direction (4th column). For the female subject, the in vivo measurements revealed (mean ± SD) FA = (35.7 ± 11.7)° and B_1^+ = (2.8 ± 0.9) μT/√kW. For the male subject, FA = (28.2 ± 10.1)° and B_1^+ = (2.3 ± 0.7) μT/√kW were observed

all acceleration factors used for the acquisition of 4CV and SAX views, the CNR mean and standard deviation, as well as the SNR$_{\text{whole-heart,mean}}$ and the SNR$_{\text{myocardium,mean}}$ mean, minimum, and maximum are summarized in Table 1 for all subjects. The mean g-factor$_{\text{whole-heart,mean}}$ of all subjects was ranging between 1.1 (R = 2) and 2.4 (R = 6) for the 4CV and between 1.1 (R = 2) and 2.5 (R = 6) for the SAX. In analogy the analysis of the g-factor$_{\text{whole-heart,max}}$ allows the assessment of the worst-case noise amplification. For R = 4 it was found to be (mean [max]) 2.2 [2.7] for the 4CV and 2.0 [2.4] for the SAX. This performance affords the acquisition of up to 4 slices per breath-hold with clinically acceptable image quality. Noise amplification associated with 1D parallel imaging increased severely with R = 6 as demonstrated in Figure 9.

4 | DISCUSSION

This work reports on the design, implementation, evaluation, and application of a modular 32-channel SGBT TX/RX array tailored for CMR at 7.0 T. The compact SGBT antenna building blocks support a flexible and reconfigurable arrangement of a high-density array that conveniently conforms to an average upper torso. The in vivo CMR feasibility study revealed good image quality, anatomic coverage, B_1^+ penetration depth, blood myocardium contrast (ie, CNR), and SNR. The overall image quality and the high spatial resolution help to reduce partial volume effects. These improvements may be particularly useful for visualizing small rapidly moving structures like valve cusps, assessing subtle anatomical features such as

FIGURE 7 End-diastolic 4CV, SAX, 2CV, and 3CV derived from 2D CINE FLASH imaging (spatial resolution = 1.1 × 1.1 × 2.5 mm³, TE = 2.09 ms, TR = 4.55 ms, GRAPPA R = 2; views per segment = 10, cardiac phases = 30, BW = 446 Hz/Px, nominal FA = 22°, V_{ref} = 520 V). Subject 1 is shown as a whole field of view (FOV) and as ROI magnified view. All seven subjects (three female, four male; age: 29-59; BMI: 23,8 ± 2,1 kg/m²) were examined without subject-specific adjustment of the SGBT antenna array geometry or the phase set
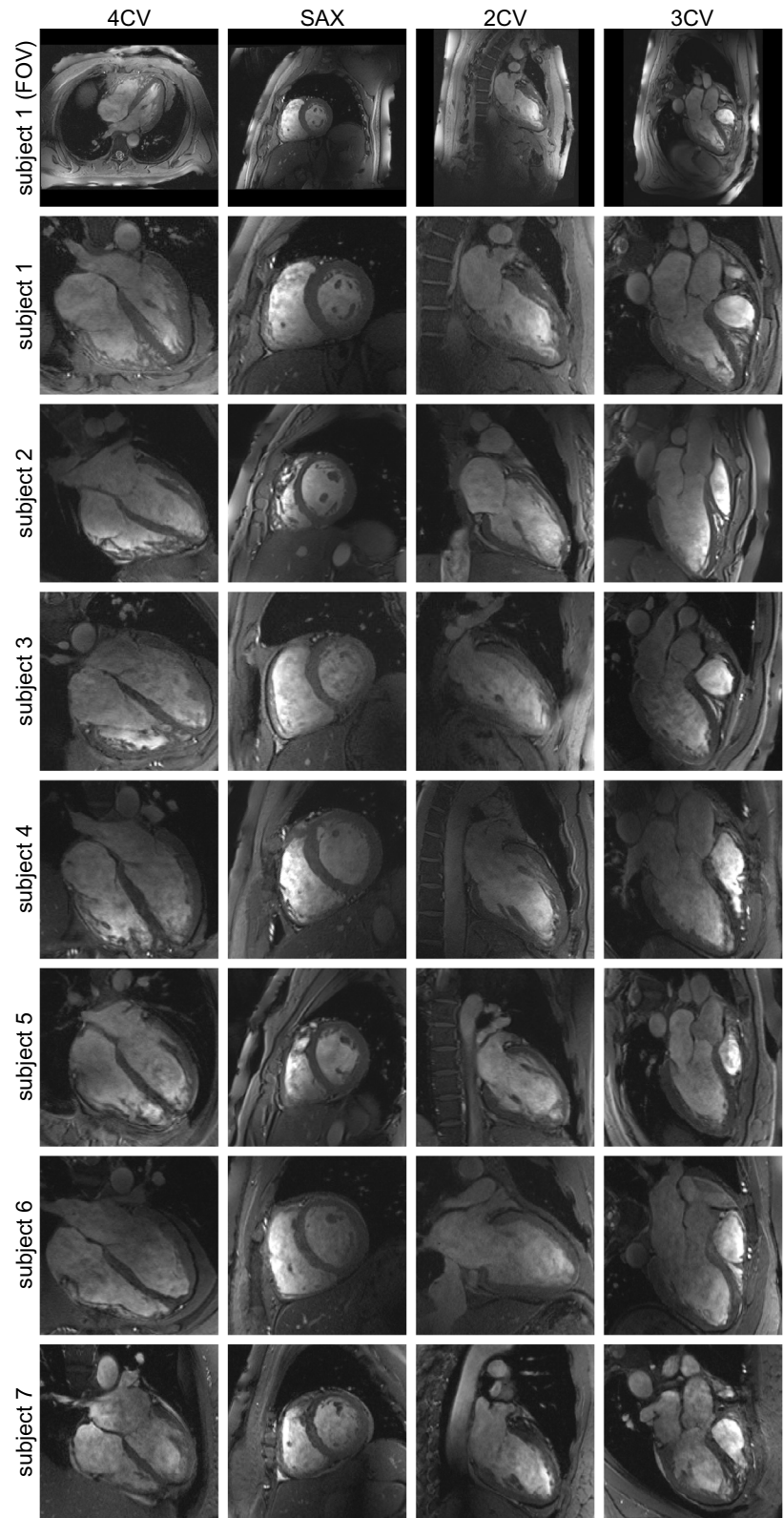
trabeculae, or extending morphologic assessment to the right ventricle including patients with congenital heart disease.[47,48]

The footprint of the SGBT building block (89.3 × 48.0 × 25.8 mm³) is reduced by 64% versus a very well established fractionated dipole (300 × 40 × 20 mm³),[11] 59% versus a bow-tie building block (150 × 70 × 40 mm³),[17] 43% versus a single-side adapted dipole (143 × 70 × 42 mm³),[16] and 87% versus a self-matched leaky-wave antenna (384 × 85 × 18 mm³).[5] The weight of the proposed building block is 156 g which is 56 g heavier compared to a 32-channel cardiac loop
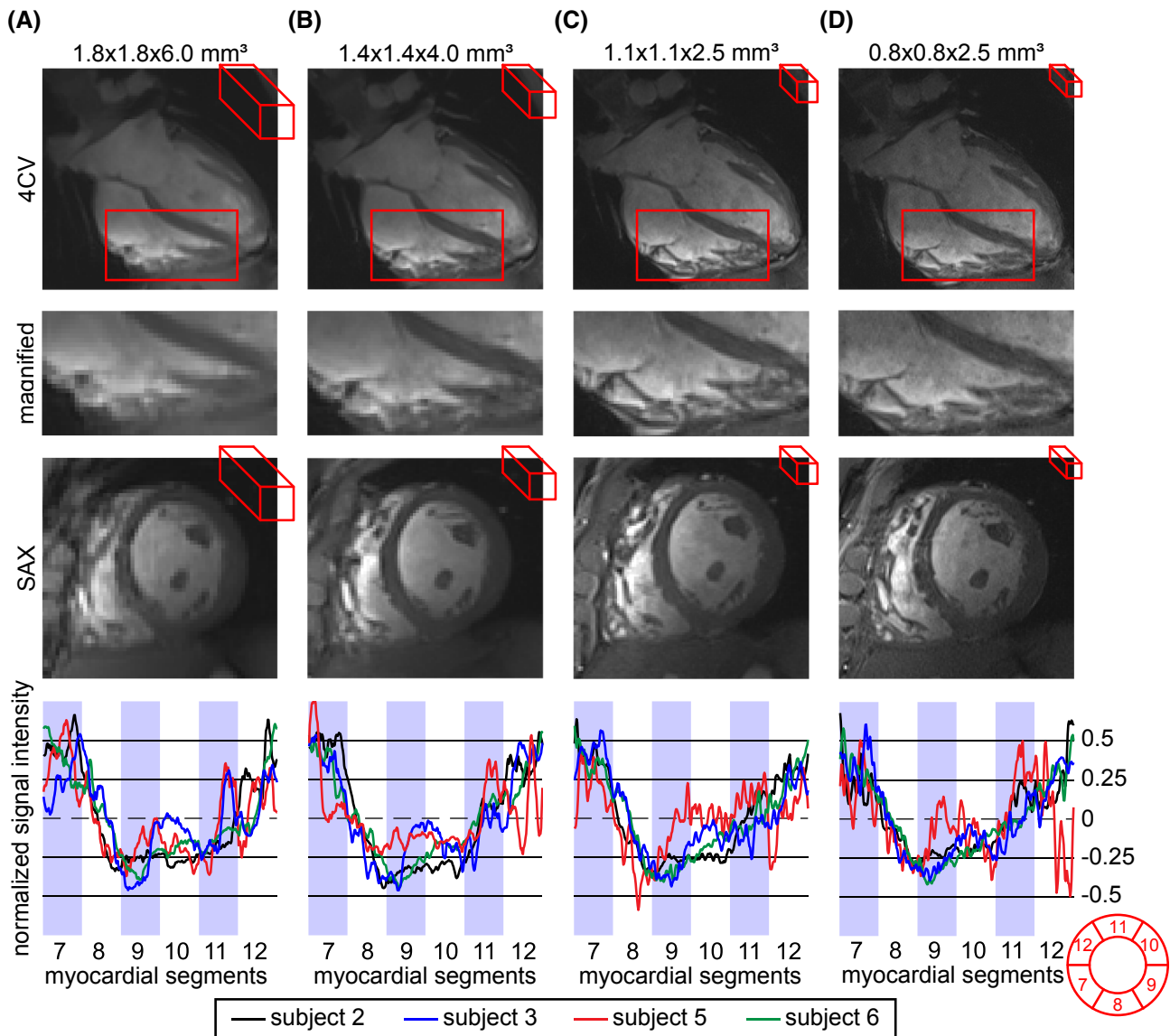
FIGURE 8 The 4CV (first row), magnified view of a section of the right ventricle (second row), and SAX view (third row) of the heart using different in-plane resolutions and slice thicknesses ranging from standard clinical protocols $1.8 \times 1.8 \times 6.0$ mm^3 (A) and $1.4 \times 1.4 \times 4.0$ mm^3 (B) to enhanced spatial resolutions $1.1 \times 1.1 \times 2.5$ mm^3 (C) and $0.8 \times 0.8 \times 2.5$ mm^3 (D). Normalized signal intensity plot (fourth row) along a circular trajectory through the myocardium of the mid-ventricular SAX views at end-diastole. For this purpose, standard segmentation of the myocardium was used[42]

element configuration with approximately 100 g (per channel), but 264 g lighter compared to a 16-channel cardiac bow-tie building block configuration exhibiting a weight of 420 g per building block (size $40 \times 150 \times 70$ mm^3 filled with D$_2$O).[6,17] As the hydrogel pad is an integral part of the SGBT antenna array, the weight of the pad adds 1.3 kg, which results in additional 81 g per channel for the anterior part of the antenna array.

The combined (Ella and Duke) B_1^+ shim procedure aimed to balance B_1^+ for both models and to provide a more generalized phase shim (α_{exc}) that supports a broader spectrum of cardiac anatomy. Individual B_1^+ optimization revealed a B_1^+ efficiency (mean $\pm$ SD [min]) of $(6.2 \pm 1.4$ [4.0]) µT/$\sqrt{kW}$

for Ella and $(5.8 \pm 2.0$ [3.0]) µT/$\sqrt{kW}$ for Duke. Previous reports on transmission field shaping of loop antenna configurations tailored for CMR at 7.0 T documented a B_1^+ efficiency of 7.4 ± 3.6 µT/$\sqrt{kW}$ (4 channel array), 5.4 ± 3.1 µT/$\sqrt{kW}$ (8 channel array), and 6.5 ± 3.1 µT/$\sqrt{kW}$ (16-channel array).[7] This translates into an at least 55% higher standard deviation and 38% higher coefficient of variation (ratio of standard deviation to mean), resulting in a reduced B_1^+ homogeneity. The maximum SAR$_{10g}$ obtained for both human voxel models does not exceed 0.3 W/kg per Watt of input power using the proposed optimized phase set. This outcome is improved or similar to previously reported RF array configurations tailored for CMRI at 7.0 T.[6,8-10,14,15,17,49] Simulation results
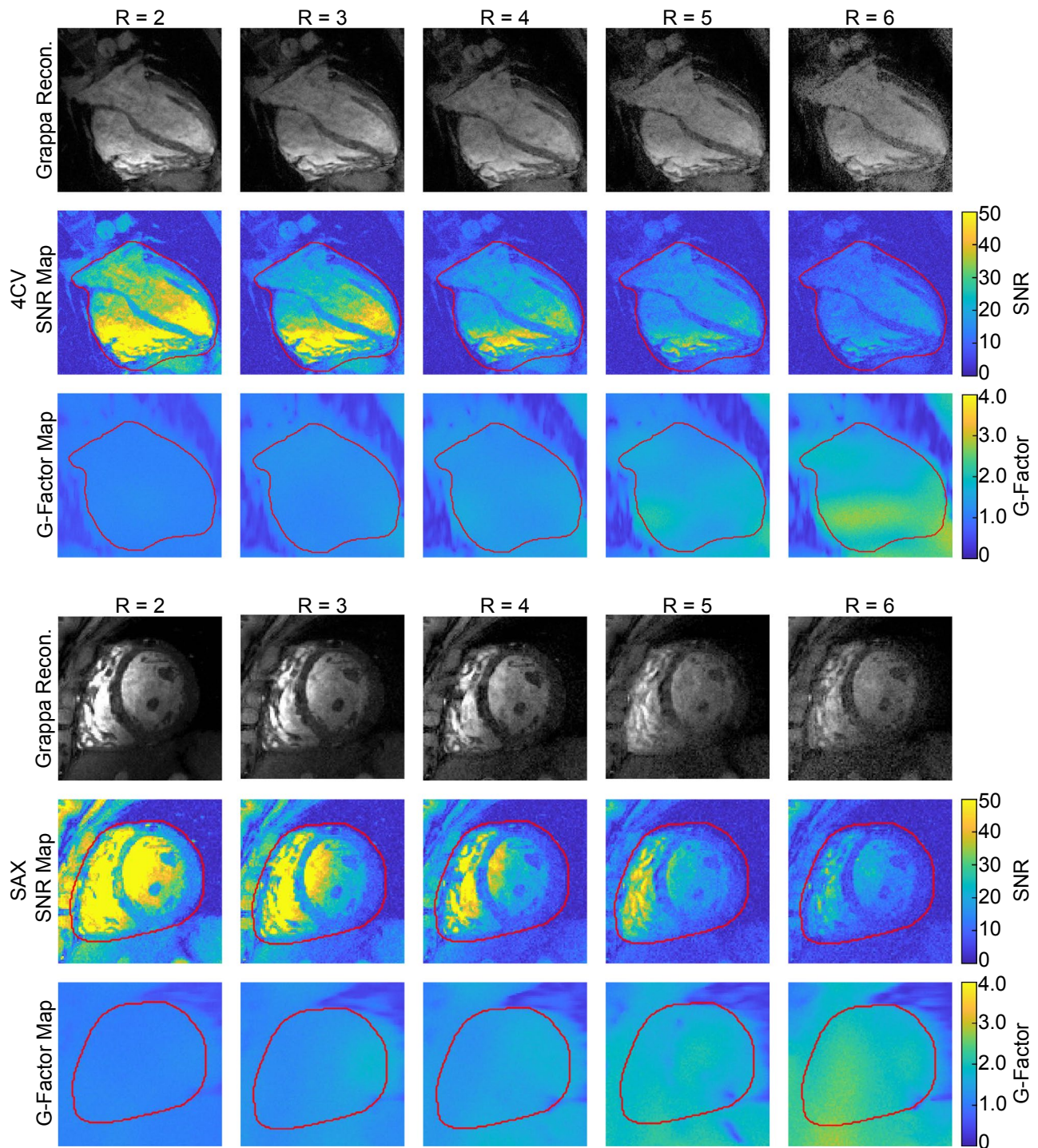
FIGURE 9 Results (female, subject 2) derived from 1D parallel imaging using acceleration factors ranging from R = 2 to R = 6. GRAPPA accelerated 2D CINE FLASH (spatial resolution = 1.1 × 1.1 × 2.5 mm³, TE = 2.5 ms, TR = 4.55 ms, views per segment = 10, BW = 446 Hz/Px, nominal FA = 22°, V_{ref} = 520V) images (first and 4th row), SNR scaled maps (second and fifth row), and g-factor map (third and sixth row) for 4CV (A) and SAX view (B); both with phase encoding direction A-P

derived for a 32-channel loop array configuration tailored for CMR at 7.0 T revealed a realistic transmit efficiency of (mean) 0.47 μT/√W for Ella and of 0.44 μT/√W for Duke and a transmit efficiency performance ratio of 73.5% for Ella and 74.9% for Duke.[6] This suggests an at least 25% improved realistic transmit efficiency at an elevated performance ratio

for the SGBT antenna array (0.59 μT/√W and 87.4% for Ella, 0.55 μT/√W, and 89.9% for Duke). The simulated B_1 superpositions for the SGBT antenna array revealed that the efficiency reduction due to intrinsic coil losses is relatively constant throughout the ROI. This presents an advantage over loop arrays, where peripheral SNR experiences a stronger

TABLE 1 4CV and SAX view analysis of GRAPPA accelerated image acquisition at increasing reduction factors (R) of four subjects (two female / two male)[a]

View	Analysis	R = 2	R = 3	R = 4	R = 5	R = 6
4CV	CNR: Mean ± Std	27.0 ± 1.9	19.5 ± 2.1	13.5 ± 1.9	9.9 ± 1.7	6.3 ± 1.7
	$SNR_{whole\text{-}heart,mean}$: Mean [Min | Max]	31.6 [29.6 | 34.2]	22.9 [20.6 | 24.7]	16.7 [15.5 | 18.8]	12.2 [10.6 | 14.9]	8.6 [7.5 | 11.0]
	$SNR_{myocardium,mean}$: Mean [Min | Max]	18.4 [16.0 | 20.7]	13.6 [10.9 | 16.1]	10.1 [8.3 | 12.6]	7.0 [5.6 | 9.7]	5.2 [4.3 | 7.2]
	g-factor$_{whole\text{-}heart,mean}$: Mean [Max]	1.1 [1.1]	1.3 [1.4]	1.5 [1.6]	1.9 [2.1]	2.4 2.7]
	g-factor$_{whole\text{-}heart,max}$: Mean [Max]	1.3 [1.4]	1.8 [2.1]	2.2 [2.7]	3.3 [4.4]	4.3 [5.2]
SAX	CNR: Mean ± Std	41.0 ± 5.5	26.9 ± 3.0	19.9 ± 2.9	12.5 ± 1.9	8.4 ± 2.3
	$SNR_{whole\text{-}heart,mean}$: Mean [Min | Max]	38.2 [32.7 | 42.4]	26.7 [24.0 | 30.4]	19.5 [16.6 | 21.8]	14.0 [11.8 | 16.9]	9.5 [8.0 | 11.7]
	$SNR_{myocardium,mean}$: Mean [Min | Max]	18.4 [16.6 | 19.6]	13.3 [11.2 | 16.9]	9.7 [8.6 | 10.9]	7.5 [6.3 | 8.5]	5.5 [4.6 | 6.1]
	g-factor$_{whole\text{-}heart,mean}$: Mean [Max]	1.1 [1.1]	1.3 [1.4]	1.5 [1.6]	1.9 [2.2]	2.5 [3.0]
	g-factor$_{whole\text{-}heart,max}$: Mean [Max]	1.3 [1.3]	1.7 [1.9]	2.0 [2.4]	2.8 [3.1]	4.0 [4.6]

[a]The data contain the contrast-to-noise ratio (CNR, mean and SD), the SNR for the whole heart and the myocardium (mean, minimum, and maximum), and the geometry factor (g-factor, mean, and max).

degradation due to coil losses compared to more central locations.[50]

The hydrogel pad promotes the performance by enhancing EMF coupling to the subject. Without the hydrogel pad and an optimized phase set, the mean B_1^+ efficiency in the heart is reduced by 45% for Ella and 39% for Duke in the same simulation setup, co-simulation, and B_1^+ shimming approach. The calculation of the optimal B_1 superposition for simulations without the hydrogel pad revealed a lower performance ratio for B_1^+ (Ella: 52%, Duke: 60%) and B_1^- (Ella: 49%, Duke: 57%).

The phantom study revealed a good agreement between simulations and measurements which is documented by a difference of 7% of the mean B_1^+ efficiency values within the defined ROI. The in vivo mean B_1^+ efficiency (female: $B_1^+ = 2.8 \ \mu T/\sqrt{kW}$, male: $B_1^+ = 2.3 \ \mu T/\sqrt{kW}$) showed a deviation of 6% and 14% versus the simulations (Ella: $B_1^+ = 2.9 \ \mu T/\sqrt{kW}$; Duke: $B_1^+ = 2.7 \ \mu T/\sqrt{kW}$) including the losses in the RF signal chain of −6.37 dB.

The small antenna building block size combined with the excellent decoupling behavior enables the setup of high-density arrays, where the building blocks can be arranged close to each other without additional decoupling measures. The compactness of the RF array benefits parallel imaging performance, where electrodynamics dictates a rapid SNR degeneration at high 1D accelerations. In recognition of the benefits of the SGBT antenna, the high-density RF array might be translated into a reduction of noise amplification in parallel imaging with the goal to preserve SNR by using 2D acceleration versus 1D acceleration.[51-53] 2D parallel imaging of the heart is only practical in the slice direction if compact RF elements such as the SGBT are used as RF arrays. The mean whole heart SNR values and CNRs of the proposed SGBT

antenna array outperform the SNR and CNR reported for a 32-channel loop array configuration with the exception of the SAX view at R = 6.[6] For the 4CV and the SAX view at R = 4 the mean $SNR_{whole\text{-}heart,mean}$ was 17 and 20 for the SGBT design versus 11 and 17 for the 32-channel loop array.[6] The mean CNR for 4CV and SAX at R = 4 were found to be 14 and 20 for the SGBT antenna array which compares to 3 and 10 for the loop array configuration.[6] The benchmarking of the mean g-factor$_{whole\text{-}heart,mean}$ revealed lower values for R ≤ 3, whereas increased reduction factors (R > 3) showed superior performance of the loop array compared to the SGBT array.[6] Due to differences in the acquisition and the image reconstruction, the results of this comparison need to be interpreted with caution and are subject to variations in the GRAPPA reconstruction.

The SGBT building block was matched and tuned to a resonance frequency of 297.2 MHz in this work. It can be conveniently adapted to a wideband configuration supporting resonance frequencies of up to 600 MHz which would facilitate CMR at magnetic field strengths of up to 14.0 T.[23,27] A high-density TX/RX array accommodating wideband SGBTs would afford ^{1}H/^{19}F CMR which would promote translational research by benefitting explorations into molecular CMR including assessment of cardiac inflammation.[54,55]

Recognizing the opportunities of adding a thermal intervention dimension to an MRI device for studying the role of temperature in biological systems and disease our high-density RF array opens a trajectory to an integrated, multi-purpose RF applicator. This applicator accommodates RF-induced heating, in vivo temperature mapping using MR thermometry, anatomic and functional MRI, and the option for x-nuclei MRI (Thermal MR).[56-61] Potential clinical applications extend beyond diagnostic cardiac imaging and can

serve as a platform to treat cardiovascular diseases, where localized RF intervention might be used, eg, terminate defective electrical pathways. Studies will reveal whether UHF-MR guided targeted RF heating for focal RF ablation can be used to terminate defective electrical pathways in the heart, and offer an alternative approach to current invasive intracardiac catheterization for the treatment of tachycardia.

5 | CONCLUSIONS

To conclude, the presented high-density transceiver array supports CMR at 7.0 T using a single feeding RF power amplifier mode without the need for subject-specific shimming or coil adjustments for the considered BMI range. The proposed cardiac TX/RX array is compatible with a multiple feeding RF power amplifier mode and contributes to the technological basis for the future clinical assessment of parallel transmit techniques designed for cardiac MR at ultrahigh magnetic fields. This work demonstrated the feasibility of the proposed modular TX/RX array for cardiac MR but the range of applications can be extended to renal imaging, abdominal imaging, pelvic imaging, thorax, and lumbar spine imaging, as well as other large-volume imaging MR applications by reconfiguring the SGBT building block-based array. With appropriate multi-transmit systems that offer more than today's state-of-the-art 8 or 16 TX channels, one might envisage the implementation of cardiac coil arrays with 32 and more TX/RX elements with the ultimate goal to break ground for many elements upper torso or body RF coil array.

DATA AVAILABILITY STATEMENT
The antenna model with the manufacturing tool models, the transmission field shaping approach, and parts of the image reconstruction and post-processing of this study are openly available at https://doi.org/10.17605/OSF.IO/NGHFS.

ORCID
Thomas Wilhelm Eigentler https://orcid.org/0000-0001-8252-450X
Andre Kuehne https://orcid.org/0000-0002-4133-5056
Laura Boehmert https://orcid.org/0000-0002-8703-3133
Sebastian Dietrich https://orcid.org/0000-0002-1610-909X
Helmar Waiczies https://orcid.org/0000-0001-6651-4790
Thoralf Niendorf https://orcid.org/0000-0001-7584-6527

REFERENCES
1. Niendorf T, Schulz-Menger J, Paul K, Huelnhagen T, Ferrari VA, Hodge R. High field cardiac magnetic resonance imaging: a case for ultrahigh field cardiac magnetic resonance. *Circ Cardiovasc Imaging*. 2017;10:1-13.
2. Niendorf T, Paul K, Oezerdem C, et al. W(h)ither human cardiac and body magnetic resonance at ultrahigh fields? Technical advances, practical considerations, applications, and clinical opportunities. *NMR Biomed*. 2016;29:1173-1197.
3. Padormo F, Beqiri A, Hajnal JV, Malik SJ. Parallel transmission for ultrahigh-field imaging. *NMR Biomed*. 2016;29:1145-1161.
4. Snyder CJ, DelaBarre L, Metzger GJ, et al. Initial results of cardiac imaging at 7 Tesla. *Magn Reson Med*. 2009;61:517-524.
5. Solomakha G, Svejda JT, van Leeuwen C, et al. A self-matched leaky-wave antenna for ultrahigh-field magnetic resonance imaging with low specific absorption rate. *Nat Commun*. 2021;12:1-11.
6. Graessl A, Renz W, Hezel F, et al. Modular 32-channel transceiver coil array for cardiac MRI at 7.0T. *Magn Reson Med*. 2014;72:276-290.
7. Winter L, Kellman P, Renz W, et al. Comparison of three multichannel transmit/receive radiofrequency coil configurations for anatomic and functional cardiac MRI at 7.0T: implications for clinical imaging. *Eur Radiol*. 2012;22:2211-2220.
8. Thalhammer C, Renz W, Winter L, et al. Two-dimensional sixteen channel transmit/receive coil array for cardiac MRI at 7.0 T: design, evaluation, and application. *J Magn Reson Imaging*. 2012;36:847-857.
9. Dieringer MA, Renz W, Lindel T, et al. Design and application of a four-channel transmit/receive surface coil for functional cardiac imaging at 7T. *J Magn Reson Imaging*. 2011;33:736-741.
10. Gräßl A, Winter L, Thalhammer C, et al. Design, evaluation and application of an eight channel transmit/receive coil array for cardiac MRI at 7.0T. *Eur J Radiol*. 2013;82:752-759.
11. Raaijmakers AJE, Italiaander M, Voogt IJ, et al. The fractionated dipole antenna: a new antenna for body imaging at 7 Tesla. *Magn Reson Med*. 2016;75:1366-1374.
12. Steensma B, Moortele P-F, Ertürk A, et al. Introduction of the snake antenna array: geometry optimization of a sinusoidal dipole antenna for 10.5T body imaging with lower peak SAR. *Magn Reson Med*. 2020;84:2885-2896.
13. Alon L, Lattanzi R, Lakshmanan K, et al. Transverse slot antennas for high field MRI. *Magn Reson Med*. 2018;80:1233-1242.
14. Steensma BR, Voogt IJ, Leiner T, et al. An 8-channel Tx/Rx dipole array combined with 16 Rx loops for high-resolution functional cardiac imaging at 7 T. *Magn Reson Mater Physics, Biol Med*. 2018;31:7-18.
15. Ertürk MA, Raaijmakers AJE, Adriany G, Uğurbil K, Metzger GJ. A 16-channel combined loop-dipole transceiver array for 7 Tesla body MRI. *Magn Reson Med*. 2017;77:884-894.

16. Raaijmakers AJE, Ipek O, Klomp DWJ, et al. Design of a radiative surface coil array element at 7 T: the single-side adapted dipole antenna. *Magn Reson Med*. 2011;66:1488-1497.

17. Oezerdem C, Winter L, Graessl A, et al. 16-channel bow tie antenna transceiver array for cardiac MR at 7.0 Tesla. *Magn Reson Med*. 2016;75:2553-2565.

18. Raaijmakers AJE, Luijten PR, van den Berg CAT. Dipole antennas for ultrahigh-field body imaging: a comparison with loop coils. *NMR Biomed*. 2016;29:1122-1130.

19. Lattanzi R, Sodickson DK. Ideal current patterns yielding optimal signal-to-noise ratio and specific absorption rate in magnetic resonance imaging: computational methods and physical insights. *Magn Reson Med*. 2012;68:286-304.

20. Lattanzi R, Sodickson DK, Grant AK, Zhu Y. Electrodynamic constraints on homogeneity and radiofrequency power deposition in multiple coil excitations. *Magn Reson Med*. 2009;61:315-334.

21. De Zwart JA, Ledden PJ, Kellman P, Van Gelderen P, Duyn JH. Design of a SENSE-optimized high-sensitivity MRI receive coil for brain imaging. *Magn Reson Med*. 2002;47:1218-1227.

22. Winter L, Özerdem C, Hoffmann W, et al. Design and evaluation of a hybrid radiofrequency applicator for magnetic resonance imaging and RF induced hyperthermia: electromagnetic field simulations up to 14.0 Tesla and proof-of-concept at 7.0 Tesla. Yacoub E, ed. *PLoS One*. 2013;8:e61661.

23. Eigentler TW, Winter L, Han H, et al. Wideband self-grounded bow-tie antenna for thermal MR. *NMR Biomed*. 2020;33:e4274.

24. Niendorf T, Graessl A, Thalhammer C, et al. Progress and promises of human cardiac magnetic resonance at ultrahigh fields: a physics perspective. *J Magn Reson*. 2013;229:208-222.

25. Eigentler TW, Boehmert L, Kuehne A, Wenz D, Oberacker E, Han H. Compact self grounded bow tie antenna resonator for cardiac MRI at 7.0 Tesla. In Proceedings of the 27th Annual Meeting of ISMRM, Montreal, CA, 2019. p. 0436.

26. Yang J, Kishk A. A novel low-profile compact directional ultrawideband antenna: the self-grounded bow-tie antenna. *IEEE Trans Antennas Propag*. 2012;60:1214-1220.

27. Takook P, Persson M, Gellermann J, Trefná HD. Compact self-grounded Bow-Tie antenna design for an UWB phased-array hyperthermia applicator. *Int J Hyperth*. 2017;33:387-400.

28. Trefná HD, Ström A. Hydrogels as a water bolus during hyperthermia treatment. *Phys Med Biol*. 2019;64:115025.

29. Christ A, Kainz W, Hahn EG, et al. The Virtual Family—development of surface-based anatomical models of two adults and two children for dosimetric simulations. *Phys Med Biol*. 2010;55:N23-N38.

30. Athey TW, Stuchly MA, Stuchly SS. Measurement of radio frequency permittivity of biological tissues with an open-ended coaxial line: part I. *IEEE Trans Microw Theory Tech*. 1982;30:82-86.

31. IT'IS Foundation. *Tissue Properties Database V4.0*. Zürich: IT'IS Foundation. https://itis.swiss/virtual-population/tissue-properties/overview/.

32. Lemdiasov RA, Obi AA, Ludwig R. A numerical postprocessing procedure for analyzing radio frequency MRI coils. *Concepts Magn Reson Part A*. 2011;38A:133-147.

33. Kuehne A, Waiczies H, Niendorf T. Massively accelerated VOP compression for population-scale RF safety models. In Proceedings of the 25th Annual Meeting of ISMRM, Honolulu, HI, 2017. p. 0478.

34. Eichfelder G, Gebhardt M. Local specific absorption rate control for parallel transmission by virtual observation points. *Magn Reson Med*. 2011;66:1468-1476.

35. Kuehne A, Goluch S, Waxmann P, et al. Power balance and loss mechanism analysis in RF transmit coil arrays. *Magn Reson Med*. 2015;74:1165-1176.

36. Lakshmanan K, Cloos M, Brown R, Lattanzi R, Sodickson DK, Wiggins GC. The "loopole" antenna: a hybrid coil combining loop and electric dipole properties for ultra-high-field MRI. *Concepts Magn Reson Part B, Magn Reson Eng*. 2020;2020:1-9.

37. Georgakis IP, Polimeridis AG, Lattanzi R. A formalism to investigate the optimal transmit efficiency in radiofrequency shimming. *NMR Biomed*. 2020;33:1-18.

38. Yarnykh VL. Actual flip-angle imaging in the pulsed steady state: a method for rapid three-dimensional mapping of the transmitted radiofrequency field. *Magn Reson Med*. 2007;57:192-200.

39. Dietrich S, Aigner CS, Kolbitsch C, et al. 3D Free-breathing multichannel absolute mapping in the human body at 7T. *Magn Reson Med*. 2021;85:2552-2567.

40. Kellman P, McVeigh ER. Image reconstruction in SNR units: a general method for SNR measurement. *Magn Reson Med*. 2005;54:1439-1447.

41. Kramer CM, Barkhausen J, Bucciarelli-Ducci C, Flamm SD, Kim RJ, Nagel E. Standardized cardiovascular magnetic resonance imaging (CMR) protocols: 2020 update. *J Cardiovasc Magn Reson*. 2020;22:17.

42. Cerqueira MD, Weissman NJ, Dilsizian V, et al. Standardized myocardial segmentation and nomenclature for tomographic imaging of the heart. *J Cardiovasc Magn Reson*. 2002;4:203-210.

43. Griswold MA, Jakob PM, Heidemann RM, et al. Generalized autocalibrating partially parallel acquisitions (GRAPPA). *Magn Reson Med*. 2002;47:1202-1210.

44. Hansen MS, Beatty P. ISMRM 2014 Sunrise Course on Parallel Imaging. ISMRM 22. Annual Meeting. https://github.com/hansenms/ismrm_sunrise_matlab. Published 2014.

45. Robson PM, Grant AK, Madhuranthakam AJ, Lattanzi R, Sodickson DK, McKenzie CA. Comprehensive quantification of signal-to-noise ratio and g-factor for image-based and k-space-based parallel imaging reconstructions. *Magn Reson Med*. 2008;60:895-907.

46. Meliadò EF, van den Berg CAT, Luijten PR, Raaijmakers AJE. Intersubject specific absorption rate variability analysis through construction of 23 realistic body models for prostate imaging at 7T. *Magn Reson Med*. 2019;81:2106-2119.

47. von Knobelsdorff-Brenkenhoff F, Tkachenko V, Winter L, et al. Assessment of the right ventricle with cardiovascular magnetic resonance at 7 Tesla. *J Cardiovasc Magn Reson*. 2013;15:1-9.

48. Al-Wakeel-Marquard N, Ferreira da Silva T, Jeuthe S, et al. Measuring myocardial extracellular volume of the right ventricle in patients with congenital heart disease. *Sci Rep*. 2021;11:1-9.

49. Boehmert L, Kuehne A, Waiczies H, et al. Cardiorenal sodium MRI at 7.0 Tesla using a 4/4 channel 1 H/ 23 Na radiofrequency antenna array. *Magn Reson Med*. 2019;82:2343-2356.

50. King SB, Varosi SM, Duensing GR. Eigenmode analysis for understanding phased array coils and their limits. *Concepts Magn Reson Part B Magn Reson Eng*. 2006;29B:42-49.

51. Ohliger MA, Grant AK, Sodickson DK. Ultimate intrinsic signal-to-noise ratio for parallel MRI: electromagnetic field considerations. *Magn Reson Med*. 2003;50:1018-1030.

52. Wiesinger F, Boesiger P, Pruessmann KP. Electrodynamics and ultimate SNR in parallel MR imaging. *Magn Reson Med*. 2004;52:376-390.

53. Niendorf T, Hardy CJ, Giaquinto RO, et al. Toward single breath-hold whole-heart coverage coronary MRA using highly accelerated

parallel imaging with a 32-channel MR system. *Magn Reson Med*. 2006;56:167-176.

54. Ramos IT, Henningsson M, Nezafat M, et al. Simultaneous assessment of cardiac inflammation and extracellular matrix remodeling after myocardial infarction. *Circ Cardiovasc Imaging*. 2018;11:1-13.

55. Rothe M, Jahn A, Weiss K, et al. In vivo 19 F MR inflammation imaging after myocardial infarction in a large animal model at 3 T. *Magn Reson Mater Physics, Biol Med*. 2019;32:5-13.

56. Oberacker E, Kuehne A, Oezerdem C, et al. Radiofrequency applicator concepts for thermal magnetic resonance of brain tumors at 297 MHz (7.0 Tesla). *Int J Hyperth*. 2020;37:549-563.

57. Ji Y, Winter L, Navarro L, et al. Controlled release of therapeutics from thermoresponsive nanogels: a thermal magnetic resonance feasibility study. *Cancers*. 2020;12:1380.

58. Han H, Eigentler TW, Wang S, et al. Design, implementation, evaluation and application of a 32-channel radio frequency signal generator for thermal magnetic resonance based anti-cancer treatment. *Cancers (Basel)*. 2020;12:1720.

59. Winter L, Oezerdem C, Hoffmann W, et al. Thermal magnetic resonance: physics considerations and electromagnetic field simulations up to 23.5 Tesla (1GHz). *Radiat Oncol*. 2015;10:201.

60. Han H, Oberacker E, Kuehne A, et al. Multi-channel RF supervision module for thermal magnetic resonance based cancer therapy. *Cancers (Basel)*. 2021;13:1001.

61. Oberacker E, Diesch C, Nadobny J, et al. Patient-specific planning for thermal magnetic resonance of glioblastoma multiforme. *Cancers (Basel)*. 2021;13:1867.